COMSOL CONFERENCE 2019 CAMBRIDGE

Simulation of bi-material nano-second laser ablation

M. Dal[1], L. Carvalho[2], A. Semerok[2], W. Pacquentin[2], H. Maskrot[2].
1. Laboratoire PIMM, Arts et Métiers, CNRS, Cnam, HESAM Université, 151 Bd de l'hôpital 75013 Paris, France.
2. CEA, DEN/DANS/DPC/SEARS/LISL, F-91191 Gif-sur-Yvette, France.

Introduction

Among the new cleaning processes, laser ablation technique generates a great interest since 1990 and has led to industrial patents [1, 2, 3]. Number of studies have been done on this topic in United States, France, China, Japan and United Kindom. This process is based on ejection of contaminated matier consequently to energy absorption coming from laser pulses. After ablating, the matier can be collected by vacuum and insulated to avoid environment contamination. As this is a non-contact method, the treatment can be provided safely regarding contamination and as only oxide is ablated, the contamined material amount to be treated remains quite weak. Moreover, this technique is particularly suitable for metallic treatment due to its ability to the laser beam to interact only with the contamined oxide. In these conditions, the laser ablation leads to high cleaning rate [4, 6].
Nevertheless, the process has to be optimized to reduce the residual contamination level. Indeed, literature indicates several parameters limiting the treatment efficiency. One of the negative effects is the diffusion of contaminant in the bulk due to the laser heating [6] and the entrapment of contaminant in surface defects [5, 7, 8]. Both of them need an increase of the laser decontamination knowledge mainly treated experimentally at this time.
In addition to an experimental study, authors propose in this paper a numerical analysis of the process. The supposed ablation phenomena are phase explosion, mechanical fracturing and vaporization.
To reduce the scale of the numerical problem, a single pulse is studied but results will be extrapolated to real treatment conditions. The physical model and numerical assumptions will be firstly explained. After result validation, an analysis of ablation mechanisms will be proposed.

Theory / Experimental Set-up

In order to be sufficiently predictive for understanding ablation phenomenon, the present model has to consider heat transfers in both phases, fluid flow and mass transfers. Moreover, as the material is evaporating, a recoil pressure is applied at the liquid-gas boundary and the liquid boundary motion has to be considered numerically (Figure 1).

All these phenomena will be described in the next subsections.

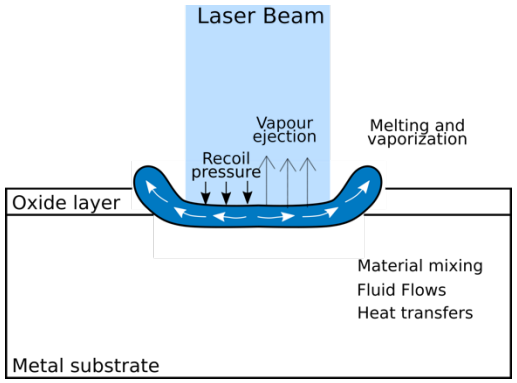

Figure 1: Scheme of laser absorption phenomena.

Governing Equations / Numerical Model / Simulation / Methods / Use of Simulation Apps

Geometrical assumption:

As the laser beam is circular and the workpiece quite large regarding the beam size R_0, it is possible to consider the problem in cylindrical coordinates system (Figure 2). Moreover, for this understanding stage, the study is focused on a single laser impact.

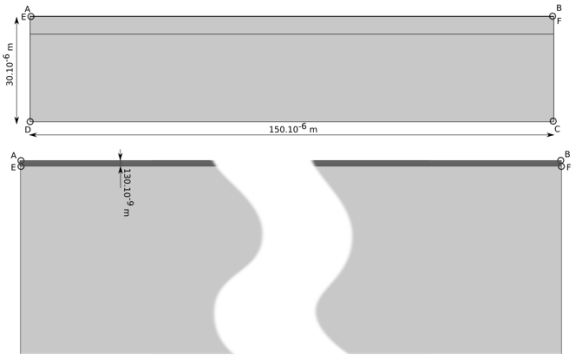

Figure 2: Simulated geometry (304L Stainless Steel: clear gray, Fe_3O_4 Iron Oxide: dark gray).

Heat transfers:

$$\rho_m c_{p_m}^{eq} \frac{\partial T}{\partial t} + \rho_m c_{p_m} \vec{v}.\overrightarrow{\nabla T} = \vec{\nabla}.\left(\lambda_m \overrightarrow{\nabla T}\right) + S_m(r,z,t)$$

Where ρ_m, $c_{p\ m}$ and λ_m are the material dependent thermal properties. T is the computed temperature and $S_m(r,z,t)$ the laser bulk power absorption set only in the oxide layer. The exponent ^{eq} indicates that the fusion latent heat is included in an equivalent [9] specific heat:

$$c_p^{eq} = c_{p_m} + \frac{L_m}{\sqrt{\pi \Delta T^2}} \exp^{\left(-\frac{(T-T_m)^2}{\Delta T^2}\right)}$$

As the oxide is not perfectly opaque, a certain amount of power is distributed in the oxide bulk. This absorption is assumed to follow a Beer-Lambert law:

$$S_m(r,z,t) = \varphi_{laser}(r,t) \exp^{-A_{Fe_3O_4}(z-z_0)} A_{Fe_3O_4}$$

With A_{Fe3O4} the oxide volume absorption, z_0 the z coordinate of A and B points (Figure 2). φ_{laser} is the spatial and temporal distribution of the laser beam.

$$\varphi_{laser}(t) = D(t) \frac{\alpha P_m}{2\, f\, \tau\, \pi\, R_0^2} \exp^{-\frac{r^2}{2R_0^2}}$$

$D(t)$ is the time distribution of the laser impulsion shown in Figure 3 and coming from experimental measurements. P_m is the mean value of laser power, R_0 the standard deviation of this Gaussian expression (with ½ factor), f the frequency and τ the pulse time duration.

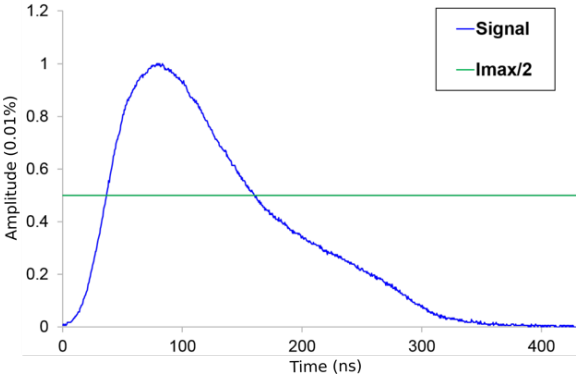

Figure 3: Measured time distribution of laser power D(t).

Boundary conditions:

- [AE] and [ED] Axial symmetry
$$-\lambda_m \overrightarrow{\nabla T}.\vec{n} = 0$$
- [AB] convection, radiation and evaporation heat losses
$$-\lambda_m \overrightarrow{\nabla T}.\vec{n} = -h_{cv}\left(T - T_{inf}\right) - \varepsilon\sigma_{sb}\left(T^4 - T_{p,inf}^4\right) - \dot{m}L_{vap}$$
- [BF], [FC] and [CD] Thermal insulation
$$-\lambda_m \overrightarrow{\nabla T}.\vec{n} = 0$$

Where, h_{cv} is a convection coefficient, ε is the material emissivity, σ_{sb} the Stefan-Boltzmann constant, $\dot{m}$ is the evaporation rate coming from Hertz-Langmuir equation [13] and L_{vap} the latent heat of vaporization.

$$\dot{m} = p_{sat}(T)\sqrt{\frac{M}{2\pi RT}}(1-\beta_r)$$

With p_{sat} the saturation pressure (Clausius-Clapeyron equation [13]:

$$p_{sat} = p_0 \exp^{\frac{ML_v}{R}\left(\frac{1}{Tv}-\frac{1}{T}\right)}$$

T_v is the boiling point, M the molar mass and p_0 the ambient pressure.

Fluid flow:

The fluid flow problem is computed through the resolution of two equations: Momentum conservation and mass conservation.

$$\rho_m\left[\frac{\partial \vec{v}}{\partial t} + (\vec{v}.\vec{\nabla})\vec{v}\right] = \vec{\nabla}.\left(pI + \mu_m(\vec{\nabla}\vec{v} + (\vec{\nabla}\vec{v})^T\right) + \overrightarrow{f_v}$$

$$\overrightarrow{\nabla}.\vec{v} = 0$$

Where the dynamic viscosity μ_m is assumed to be the same in both materials. It should be noted that the mass conservation is written here for a not compressible material and Boussinesq approximations are not made here due to the very fast time dynamics avoiding convective eddies.

Boundary conditions:

- [AE] and [ED] Axial symmetry
$$\vec{v}.\vec{n} = 0$$
- [AB] surface tension and recoil pressure
$$\sigma.\vec{n} = \gamma(T)\kappa + p_{rec}$$
- [BF], [FC] and [CD] no slip
$$\vec{v} = \vec{0}$$

With γ the liquid material surface tension, κ the local curvature of the interface and p_{rec} the recoil pressure coming from the saturation pressure and considering the retro-diffusion coefficient β_r [12].

$$p_{rec} = p_0 + p_{sat}\frac{(1+\beta_r)}{2}$$

To complete the description, the initial conditions in velocity is zero and the pressure is set to the atmospheric one. The laser evaporation thermal and mechanical phenomena are described in more detail in literature [10, 11, 13].

Chemical species transport:
As the aim is to compute the oxide residual content, the proportion of each element (steel and oxide) has to be computed. The model used here is the component conservation thanks to the Fick law:

$$\frac{\partial C}{\partial t} + \vec{v}.\overrightarrow{\nabla C} = \vec{\nabla}.\left(D_{iff}(T)\,\overrightarrow{\nabla C}\right)$$

For the whole boundaries, no material flux is considered. The diffusion coefficient $D_{iff}(T)$ is assumed to be temperature dependent through an Arrhenius law in the solid phase and related to the Stokes-Einstein approximation in the liquid [14]:

$$D_{iff}(T) = \begin{cases} D_0 e^{-\frac{Q}{RT}} & (T < T_{m_{Fe_3O_4}}) \\ \dfrac{k_b T}{6\pi a_{Eu}\mu} & (T > T_{m_{Fe_3O_4}}) \end{cases}$$

Where D_0 is the pre-exponential factor, Q is the activation energy, k_b is the Boltzmann constant and a_{Eu} is the atomic size of Europium element.
It should be noted that the diffusive properties of oxide in steel with the temperature are not very accurate. Nevertheless, as the dynamic is very fast the fluid transport is supposed to be more sensitive.

Liquid deformation and material ablation:
In this model the liquid - gas interface has to move due to the recoil pressure compensated by surface tension and due to the material withdrawal by vaporization. The former phenomena are computed form pressure equilibrium coming from fluid flow calculation ([AB] boundary condition in *Fluid flow* paragraph), thus naturally conservative in mass. The later one is coming from the mass ablated rate calculation $\dot{m}$. As this mass leaves the studied system, it has to be uncorrelated to the mass conservation.

Boundary conditions:
- [AE] , [ED] ,[BF] and [FC] no motion in the *r* direction and free displacement in the *z* direction
- [DC] free along *r* and locked along *z*
- [AB] normal velocity

$$v_b = \vec{v}.\vec{n} - \overrightarrow{v_a}.\vec{n}$$

With $\vec{v}.\vec{n}$ the conservative part coming from the fluid flow calculation and $\overrightarrow{v_a}.\vec{n}$ the normal "ablation velocity" ($\overrightarrow{v_a}.\vec{n} = \dot{m}/\rho_m$)

The resulting motion of the mesh in the domains is computed in order to optimize the mesh quality through an arbitrary *hyper-elastic* model.

Model and process parameters:
The parameters used in previous models are summarized in tables 1 and 2.

Table 1: Model Properties

Properties	*304L*	*Fe_3O_4*
λ [W/m/K]	24.5	15
ρ [kg/m^3]	8020	5180
c_p [J/kg/K]	609	621
D_0 [m^2/s]	5 10^{-6}	4.5 10^{-7}
α [%]	29	70
A [cm^{-1}]	36 10^4	32 10^4
T_m [K]	1700	1863
T_v [K]	3173	2896

Table 2: Common and process properties

Properties	*304L and Fe_3O_4*
η [Pa.s]	0.004
γ [N/m]	1.6
$\frac{\partial \gamma}{\partial T}$ [N/m/K]	$1.2\ 10^{-4}$
β_r	0.17
R_0 [m]	$32.5\ 10^{-5}$
P_m [W]	15
T_∞ [K]	293
h_{cv} [W/m^2/K]	10

Mesh properties and time step:
This problem has the particularity to be multi-scales in space and in time. In other words, the oxide layer is *130 nm* thick and the whole simulated piece is *30 µm* thick (figure 2) and the pulse duration is *150 ns* (figure 3) whereas the process period is *50 µs*. Thus, the time and space discretizations have to be chosen carefully.
Firstly, in order to consider correctly the whole laser pulse, a time step of *5 ns* is set during the pulse and *10 ns* during the cooling. Secondly, the oxide layer is spatially meshed with triangular *10 nm* elements.
After a mesh convergence analysis, this configuration seems to allow correct computation of laser absorption and oxide concentration calculation.
In the rest of the element sizes growth with a factor of 1.1 (Figure 4).

In order to reduce the Degrees Of Freedom to be solved, a linear interpolation is set in elements for all physics. The numerical problem is thus composed by more of 2500000 DOF, solved with 2x8@2.4GHz CPU in approximately 4 hours.

Results and discussion

Before presenting results, the aim of this numerical analysis has to be recalled. This model is made to predict the ablated material amount and to understand ablation phenomena. The first part of the results is the model validation regarding similar experiment. In a second step, the ablation phenomena will be analyzed in the current process parameter range.

Model validation
Firstly, the thermal field can be validated trough oxide ablation amount and melted zone comparisons with experiments. The figure 5 is an extrapolate 3D view showing oxide concentration decrease with the time during one spot laser processing. It can be observed that the ablated zone remains constant after *500 ns*, i.e. few

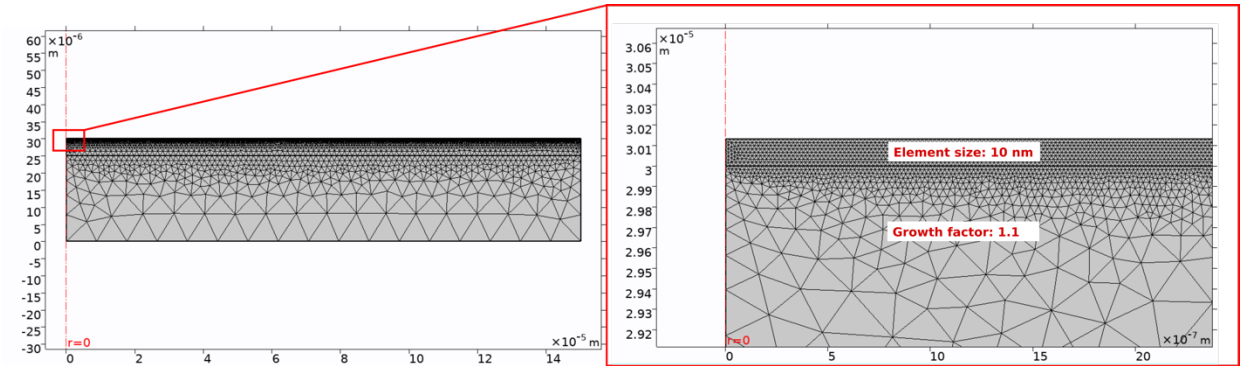

Figure 4: Mesh definition.

hundred nanoseconds after the laser pulse. Two mechanisms are responsible to the oxide amount decrease in the center part, the material removing due to evaporation and the lateral fluid motion involved by recoil pressure.

The isolevel lines indicate the fusion and vaporization temperatures. The larger one can be compared to the experimental melted zone (figure 6).

In order to validate the thermal field, numerical key temperatures (melting and vaporization) are compared to experimental picture in figure 6. A particular caution has been taken to scales equality between experiment and simulation results. The experimental picture shows three different areas, the ablated zone (lighter zone is the metal), oxide melted zone where the initial roughness seems to be modified and the solid oxide zone. The comparison indicates that the ablated zone corresponds to material part which is higher than the boiling point and the melted

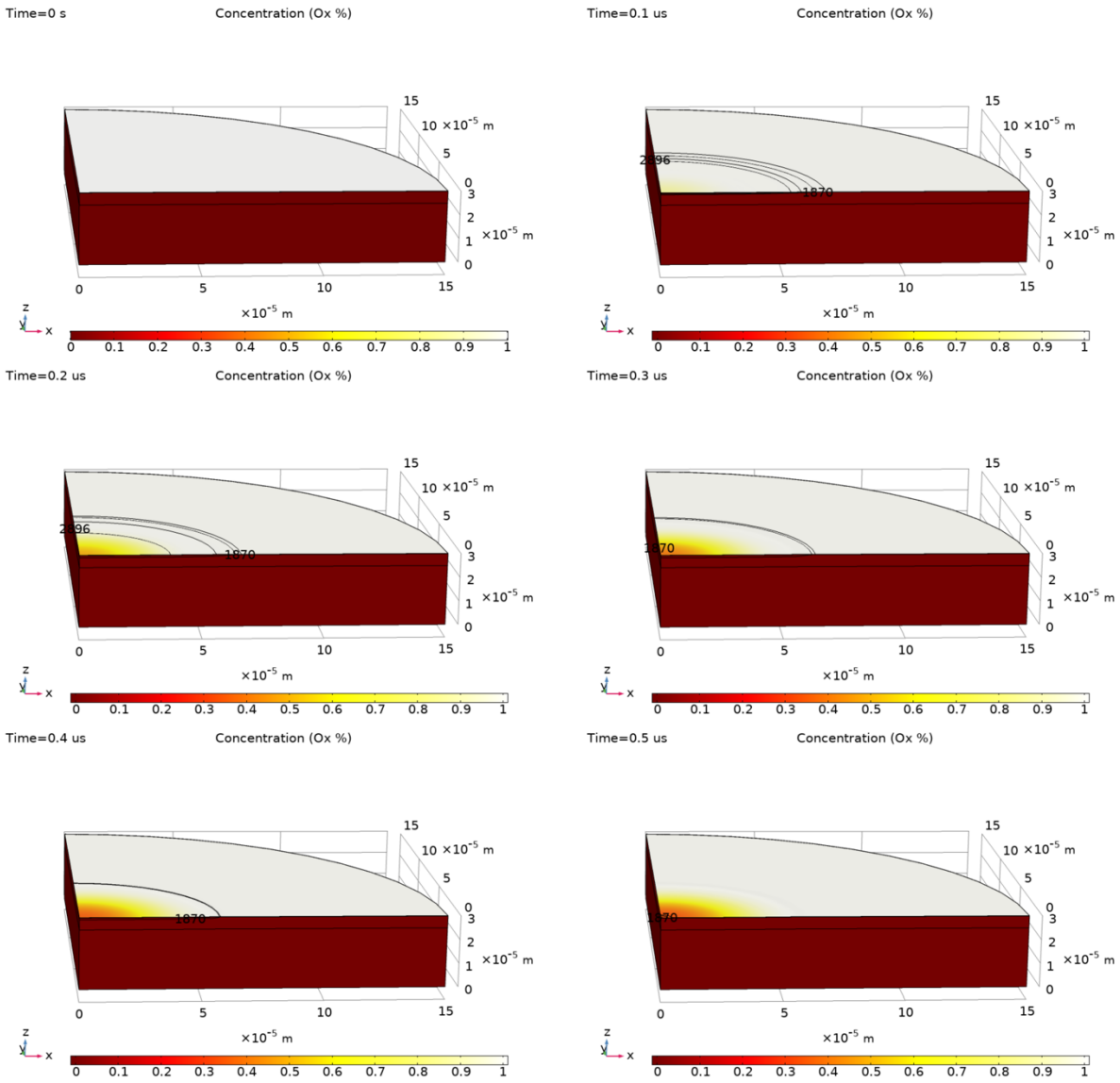

Figure 5: Dynamics of oxide removal.

oxide limit is also consistent with calculated melted zone.

In addition to this upper view analysis, the melted thickness was measured on transmission electronic microscopy pictures. The experimental thickness is estimated to 0.7 µm whereas the numerical model predicts 1.2 µm. This discrepancy can be explained by the uncertainties on material properties at high temperature. Indeed, in the model, thermal properties are different for oxide and metal, but not temperature dependent. Moreover, as the phase change is very fast, it is quite difficult to detect the transition zone accurately on TEM pictures. The experimental information is probably slightly underestimated.

The computed minimal oxide residual concentration is close to 28 %. As the measured initial content of contaminant was 1 % in the oxide, we can estimate its residual concentration as 0.28 % numerically. This content has also been measured experimentally to 0.2 % (by GDMS).

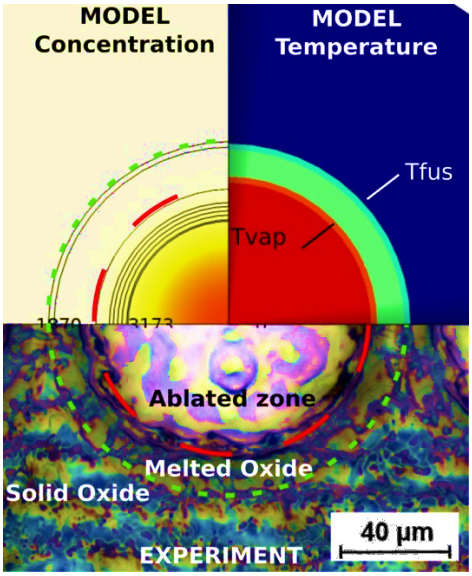

Figure 6: Experiment and numerical melted and evaporated zones

As the thermal and species fields are quite well estimated numerically, the model is supposed to be sufficiently predictive to allow understanding of the oxide layer withdrawal.

Oxide layer removal analysis:

In this part, the previous model will be used to explain phenomena occurring during oxide layer ablation. The most probable reasons of oxide withdrawal are:

— phase explosion,
— mechanical fracturing,
— vaporization.

The first one appears when the metal start to evaporated before oxide with both oxide and metal in liquid phase. The second one is similar to glass cutting, i.e. the solid oxide is broken due to its thermal expansion. The last one, is the classical evaporation process, which means that the oxide leaves the sample as vapor.

To validate or invalidate one of the previous ablation origins, the temperature evolution seems to be crucial information. The time evolution of point A and E temperatures are plotted in figure 7. The different material melting and boiling points are added to the plot. The intersections of lines and temperature curves indicate when each phase start to melt and evaporate.

This figure indicates that the oxide melts and evaporates before metal. Moreover, the metal start to melt nearly when the oxide starts to evaporate. When the metal start to evaporates, the calculated evaporation rate of oxide is more than 20 times higher than metal. This fact indicates that the phase explosion is the weakest likely assumption.

In addition to this analysis, the high evaporation rate indicates the vaporization is a sensitive phenomenon in this context. For instance and for this case, with an evaporation radius equal to the laser beam radius ($32\ \mu m$) during approximately $100\ ns$ the ablated mass during $1.44\ 10^6$ pluses (experimental conditions) is computed to $5.1\ mg$. The experimentally measured vaporized mass is estimated to $3.3\ mg$. The gap between these two values is mainly due to the context and assumptions. Indeed, numerically, the ablated mass of one pulse is multiplied by the number of experimental spot while the experimental data concerns overlapped spots (80 %). Thus, the two evaporation cases are not perfectly similar, in the numerical case, only oxide is ablated, whereas in

the experiment, a part of previously ablated area is reheated. As the oxide absorbs more energy than metal, the evaporation considered numerically is higher.

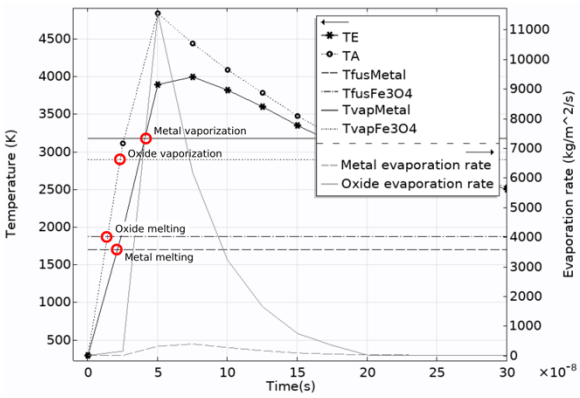

Figure 7: Temperature and evaporation rate evolution with time on points A and E (Figure 1).

Conclusions

As a conclusion, an ablation model has been done considering thermal, fluid flows and species effects. As the experimental context is quite extreme, the experimental validation is difficult. Nevertheless, the few information compared between the model and experiment results allow to be quite confident with the simulation. It provides a lot of information to analyze and leads to propose interpretation of the most likely mechanism occurring in our ablation case.

References

1. W.H. Kasner, T.A.Wojcik, H.E. Feree, Laser decontamination method, *Patent EP0091646B1* (1986).
2. S. Shuttleworth, M.R. Chandratillake, V.J. Robinson, Material removal by laser ablation, *Patent WO199502798 6A1* (1995)
3. J.P Cartry, G. Clar, A. Martin, Apparatus for working by laser, especially for the decontamination of a pipe of a nuclear reactor, *US Patent 5256848* (1993).
4. A. Leontyev, Laser decontamination and cleaning of metal surfaces: modelling and experimental studies, *PhD thesis*, Université Paris Sud - Paris XI, (2011).
5. Ph. Delaporte, M. Gastaud, W. Marine, M. Sentis, O. Uteza, P. Thouvenot, J.L. Alcaraz, J.M. Le Samedy, D. Blin, Dry excimer laser cleaning applied to nuclear decontamination, *Applied Surface Science*, **208**, 298–305 (2003).
6. R.L. Demmer, R.L. Ferguson, *Testing and evaluation of light ablation decontamination, Technical report*, EG and G Idaho, Inc., Idaho Falls, (1994).
7. Nuclear Energy Agency, R&D and Innovation Needs for Decommissioning Nuclear Facilities (2014).
8. A.J. Potiens, J.C. Dellamano, R. Vicente, M.P. Raele, N.U. Wetter, E. Landulfo, Laser decontamination of the radioactive lightning rods, *Radiation Physics and Chemistry*, **95**, 188-190 (2014).
9. C. Bonacina, G. Comini, A. Fasano, M. Primicerio, Numerical solution of phase-change problems, *International Journal of Heat and Mass Transfer*, **16** 1825-1973 (1973).
10. C.J. Knight, Theoretical modeling of rapid surface vaporization with back pressure, *AIAA Journal*, **17**, 5p (1979).
11. A. Matsunawa, V. Semak, The simulation of front keyhole wall dynamics during laser welding, *Journal of Physics D: Applied Physics*, **30**, 798-809 (1997).
12. K. Hirano, R. Fabbro, M. Muller, Experimental determination of temperature threshold for melt surface deformation during laser interaction on iron at atmospheric pressure, *J. Phys. D. Appl. Phys.*, **44**, 435402 (2011).
13. A.A. Samokhin, *Effect of Laser Radiation on Absorbing Condensed Matter*, Nova Science Publishers (1990).
14. A.D. Pasternak, D.R. Olander, Diffusion in liquid metals, *AIChE Journal*, **13(6)** 1052–1057 (1967).